ETH zürich

ETH Library

Ab initio calculation of femtosecond-time-resolved photoelectron spectra of NO2 after excitation to the A-band

Journal Article

Author(s):
Tehlar, Andres; von Conta, Aaron; Arasaki, Yasuki; Takatsuka, Kazuo; Wörner, Hans Jakob

Publication date:
2018-07-21

Permanent link:
https://doi.org/10.3929/ethz-b-000279735

Rights / license:
In Copyright - Non-Commercial Use Permitted

Originally published in:
The Journal of Chemical Physics 149(3), https://doi.org/10.1063/1.5029365

This page was generated automatically upon download from the ETH Zurich Research Collection.
For more information, please consult the Terms of use.

This article may be downloaded for personal use only. Any other use requires prior permission of the author and AIP Publishing.

This article appeared in *J. Chem. Phys.* **149,** 034307 (2018) and may be found at https://doi.org/10.1063/1.5029365.

Ab-initio calculation of femtosecond-time-resolved photoelectron spectra of NO_2 after excitation to the A-band

Andres Tehlar,[1] Aaron von Conta,[1] Yasuki Arasaki,[2] Kazuo Takatsuka,[2] and Hans Jakob Wörner[1, a)]

[1)] *Laboratory for Physical Chemistry, ETH Zürich, Wolfgang-Pauli-Strasse 10, CH-8093 Zürich, Switzerland*

[2)] *Fukui Institute for Fundamental Chemistry, Kyoto University, Sakyo-ku, Kyoto 606-8103, Japan*

(Dated: 12 June 2018)

We present calculations of time-dependent photoelectron spectra of NO_2 after excitation to the A-band for comparison with XUV time-resolved photoelectron spectroscopy. We employ newly calculated potential energy surfaces of the two lowest-lying coupled $^2A'$ states obtained from multi-reference configuration-interaction calculations to propagate the photo-excited wave packet using a split-step-operator method. The propagation includes the nonadiabatic coupling of the potential surfaces as well as the explicit interaction with the pump pulse centered at 3.1 eV (400 nm). A semiclassical approach to calculate the time-dependent photoelectron spectrum arising from the ionization to the eight energetically lowest-lying states of the cation allows us to reproduce the static experimental spectrum up to a binding energy of 16 eV and enables direct comparisons with XUV time-resolved photoelectron spectroscopy.

[a)] Electronic mail: hwoerner@ethz.ch

I. INTRODUCTION

Conical intersections play a central role in the photochemistry of most molecules, determining the pathway of reactions in molecules of all sizes ranging from DNA to small molecules, such as 1,3-cyclohexadiene, iodomethane or nitrogen dioxide. The latter is a prototypical system to study the effect of a conical intersection, which, in NO_2, connects the energetically lowest lying excited state to the ground state. Its presence leads to complex femtosecond dynamics in the electronically excited state after excitation around 400 nm and enables the dissociation of the molecule after internal conversion to the ground-state surface. These properties as well as the limited number of electrons and nuclei make NO_2 an ideal candidate to benchmark high-level ab-initio calculations against suitable experimental observables. The spectroscopic properties of NO_2 have been determined with high accuracy[1–9]. However, femtosecond time-resolved experiments have only recently become possible with the introduction of multiphoton time-resolved photoelectron spectroscopy (MP-TRPES)[10–15] (for a review, see[16]) and time-resolved high-harmonic spectroscopy (TRHHS)[17–22]. Whereas these techniques could be realized with state-of-the-art femtosecond lasers, their interpretation is sometimes challenging because of the high peak intensities associated with femtosecond laser pulses. The previous experiments on NO_2 nicely illustrate this statement because substantially different observations were reported with respect to the dynamics created by single-photon excitation at 400 nm. For example, oscillations in the yield of NO^+ and slow (near-zero eV) photoelectrons were reported with periods ranging from 500 to 750 fs, in pump-probe experiments involving 400-nm and 267-nm laser pulses[10,13,14]. In contrast to this, oscillations with a period of $\sim$220 fs were observed in time-resolved mass spectrometry[23]. Time-resolved high-harmonic spectroscopy revealed 1-2 oscillations with a period close to 100 fs[18–20]. Notably, all of these observations were attributed to dynamics induced by single-photon excitation in the vicinity of 400 nm. A distinctive feature of the TRHHS results[18] was the unequivocal demonstration of dominant single-photon excitation through the wavelength dependence of the signals, i.e. the presence of the characteristic few-picosecond dissociation time scale of NO_2 for excitation above the dissociation threshold at 3.23 eV (398 nm) and its absence for excitation below the threshold. This hallmark of single-photon excitation in NO_2 has not been reported in any of the MP-TRPES experiments, although a small number of studies based on coincidence detection have established

the contribution of single-photon excitation at long pump-probe delays ($> 400 - 500$ fs)[12,14]. Recently, some of the present authors have applied extreme-ultraviolet (XUV)-TRPES to the same excited-state dynamics in NO_2[24]. The application of single-photon ionization removes the complications induced by the high peak intensities and reveals the genuine dynamics of the photo-excited molecular system over its complete reaction path. The main motivation for the present (theoretical) work was the interpretation of these novel experimental results, as well as a possible future modelling of TRHHS or MP-TRPES results.

On the theoretical side, NO_2 has been also been extensively studied. Potential-energy surfaces of the energetically lowest lying electronic states of the neutral molecule[25–33] and the cation[34,35] have been calculated for a long time and have reached a high level of accuracy. The surfaces with the highest density of points so far were Davidson-corrected multi-reference configuration-interaction (MRCI) calculations with the Dunnings correlation-consistent polarized valence quadruple zeta (cc-pVQZ) basis set[36] for the two lowest electronic states of the neutral molecule[32] and MRCI cc-pVDZ[36] calculations for the cationic molecule[35]. Some of the surfaces have been used to calculate time-dependent wave packets after excitation, lea to insights into the short-time dynamics[37] and enabling the calculation of experimental observables, such as photoelectron spectra and photoelectron angular distributions[38]. However, due to the strong dependence of the potential energies of the different states of NO_2 on the nuclear coordinates (both in the cation as well as in the neutral molecule), there are many accessible cationic states for a given binding energy after excitation at 400 nm. This makes high-level calculations of photoelectron spectra very expensive. In this work, we extend previous wave-packet calculations of two of the present authors[37,38] to a larger grid, enabling us to accurately describe the photodissociation. Simultaneously, we improve the level of theory from complete active space self-consistent field (CASSCF) to MRCI, which allows us to reach quantitative accuracy with respect to the dissociation threshold. We present the results of full-dimensional quantum-mechanical wave-packet calculations on these novel surfaces. Subsequently, we report the calculation of time-dependent photoelectron spectra for comparison with recent experimental data from XUV-TRPES[24] in an extended range of binding energies for the channels leading to the two lowest lying states of $^1A'$, $^1A''$, $^3A'$ and $^3A''$ character of the cationic molecule within a semiclassical model.

II. METHOD

A. Calculation of potential-energy surfaces

To describe the nuclear arrangement of NO_2, we use three different coordinate systems: internal coordinates, Jacobi coordinates[39], and Cartesian coordinates (see figure 1).

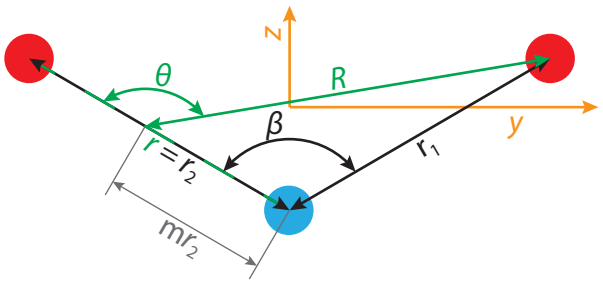

FIG. 1. Coordinate systems for NO_2: Black: internal coordinates with the NO bond lengths r_1 and r_2, as well as the bond angle β. Green: Jacobi coordinates r, R, and θ. The coordinate R is measured from the center of mass along the NO-bond, i.e. $r_2 m = r_2 m_O / (m_O + m_N)$ from the nitrogen nucleus, where m_O and m_N are the atomic masses of oxygen and nitrogen, respectively. Orange: molecular-frame Cartesian coordinates. The molecule lies in the yz-plane. The origin is located in the center of charge and z is pointing along the β-angle bisector.

The potentials, which are used in the wave-packet calculations and the photoelectron calculations, are determined on the following grid:

$$r = 0.9\text{Å} + 2.625 \cdot 10^{-2}\text{Å}\ i_r, \quad \text{with } i_r = 0, \ldots, 90, \tag{1}$$

$$R = 0.484375\text{Å} + 2.21875 \cdot 10^{-2}\text{Å}\ i_R, \quad \text{with } i_R = 0, \ldots, 155, \tag{2}$$

$$\theta = 180^\circ - (45/64)^\circ\, i_\theta, \quad \text{with } i_R = 0, \ldots, 250. \tag{3}$$

This grid consists of 3.6 million points. For the electronic states of the neutral molecule, 28250 points were calculated and the remaining ones interpolated. The calculated points were not equidistant. Their density was chosen to be high in the potential minimum, around the conical intersection, and where problems with the interpolation on the grid occurred. The number of points was increased until satisfactory potential surfaces up to an energy of

3.5 eV of the $(1)^2A'$ state above the lowest energy in the grid were achieved. The quantum-chemistry calculations were performed using the Molpro suite[40]. We first determined the two-state-averaged wave functions with the MC-SCF approach with a CAS(13,10)[41,42] in a simplified configuration, namely $r_1^{\text{init}} = r_2^{\text{init}} = 1/2\,(r_1 + r_2)$. This was taken as an initial guess for a two-state-averaged CASSCF(13,10) calculation at the final configuration with a subsequent MRCI(13,10)[43–45] calculation. Here, (13,10) refers to the chosen active space: we used 10 open orbitals with 13 active electrons. In the case of CASSCF calculations, the five orbitals with the lowest energies were closed. For the MRCI calculation, two orbitals were closed and three were frozen (core) orbitals. All calculations used the optimized augmented Dunnings correlation-consistent polarized valence quadruple zeta (aug-cc-pVQZ) basis set[36]. The output was checked for convergence problems and, in case of errors, recalculated. Configurations which could not be converged or resulted in energies which were significantly different from the surrounding points were excluded. For the potential surfaces of the neutral states, we tried to calculate the potential at 29174 grid points (i.e. 924 calculations did not converge). For the potential surfaces of the cationic states, the number of points was decreased (between 5864 and 6167 points), as they were not needed for the propagation. Further details are given in appendix A.

The diabatization of the neutral adiabatic potentials was performed on the basis of a phenomenological approach[46,47] by maximizing the transition dipole moment $\mu^y_{\text{D},12}$ between the diabatic states. The reliability of this diabatization scheme has been numerically verified in ref. 46. This leads to a diabatization angle

$$\alpha_\mu = \frac{1}{2}\text{atan2}(\mu^y_{11} - \mu^y_{22},\ 2\mu^y_{12})\,, \tag{4}$$

where μ^y_{11} and μ^y_{22} are the permanent dipole moments along the y-axis of the $(1)^2\text{A}'$ and $(2)^2\text{A}'$ states, respectively, and μ^y_{12} is the transition dipole moment between them (see figure 1 for the definition of the y-axis). This method relies on the properties of the $(1)^2\text{A}_1$ and $(1)^2\text{B}_2$ states (labeled in the $\text{C}_{2\text{v}}$ symmetry of the ground state) and fails when a third state interacts significantly with these states. In these parts of the coordinate space, the mixing angle was approximated. Generally, the angles were visually inspected for cuts along θ and smoothly continued to $0, \pi/2$, or $-\pi/2$, respectively. Figure 2 illustrates the diabatization process. The treatment of areas with non-negligible coupling of a third state is further discussed in the appendix B.

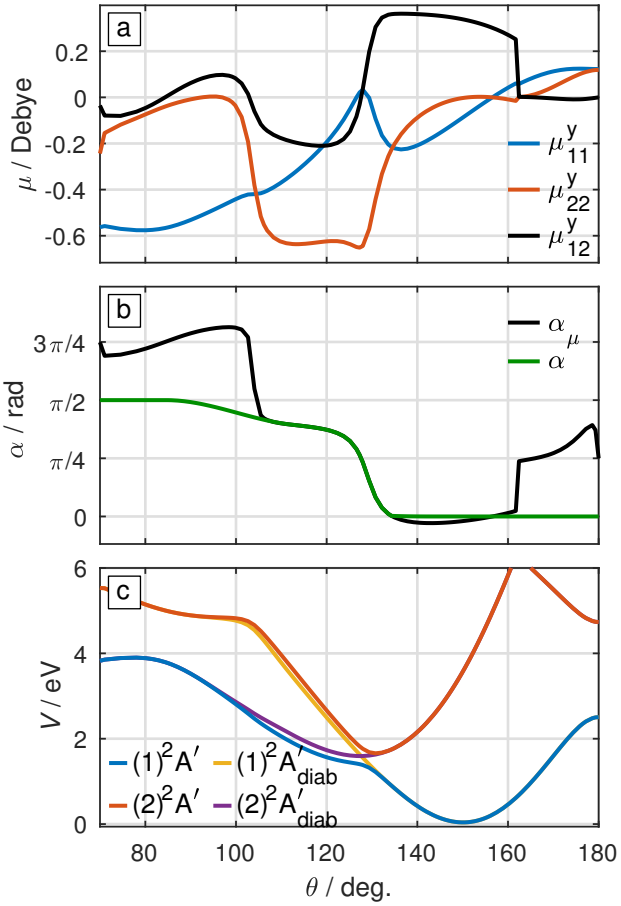

FIG. 2. Illustration of the diabatization process. All plots are cuts through the hypersurfaces of the lowest-lying electronic states of NO_2 with $r = 1.1625$ Å and $R = 1.7047$ Å. (a) Calculated permanent dipole moments of $(1)^2A'$ and $(2)^2A'$ along the y-axis (blue and red), as well as their transition dipole moment (black). (b) Mixing angles: The black curve illustrates the mixing angle calculated according to equation (4) and the green curve is the modified diabatization angle which was used in the diabatization. (c) Final result of the diabatization: The adiabatic potentials are colored in red and blue, the diabatic potentials in yellow and violet. The additional avoided crossings around $\theta = 80°$ (between the first and second adiabatic state), 105° and 165° (both between the second and third adiabatic state) were not diabatized.

The raw data attached to this paper includes the adiabatic energies, the diabatic energies and coupling constants, the permanent dipole moments and transition dipole moments in the y-direction between the two lowest $^2A'$ states of the neutral molecule, as well as the adiabatic energies of each of the two lowest $^1A'$, $^1A''$, $^3A'$, and $^3A''$ states of the cationic

molecule. The interpolation method is described in the appendix C.

B. Calculation of the vibronic wave packet

The vibronic wave packet was calculated with a split-step-operator method presented before[37]. As the wave packet is calculated on a grid, the dissociating parts of the wave function could not be fully described. Absorbing barriers were constructed[48] and tested for minimal reflection of the wave function at the edges of the grid. The optical potential has the shape

$$V_{\mathrm{opt}}(\theta, R, r) = \max(A(\theta, R, r)\,, A(\theta', R', r'))\,. \tag{5}$$

with

$$\begin{aligned} A(\theta, R, r) = \max(0, m_r\,(r - r_{\mathrm{abs}})\,, \\ m_R\,(R - R_{\mathrm{abs}})\,, m_\theta\,(\theta - \theta_{\mathrm{abs}}))\,, \end{aligned} \tag{6}$$

where $r_{\mathrm{abs}} = 3.0263$ Å$, m_r = 1.2425$ eV Å$^{-1}, R_{\mathrm{abs}} = 3.7016$ Å$, m_R = 1.1828$ eV Å$^{-1}, \theta_{\mathrm{abs}} =$ 21.7969 deg, and $m_\theta = -0.0139$ eVdeg^{-1}. The primed parameters are defined as the set of Jacobi-coordinates using the center of mass along the other bond of NO_2 (see equations B1-B3). This definition ensures that the symmetry of the generated wave packet is not broken due to the absorption. The initial ground state wave function was found by calculating an energy spectrum of a Gaussian centered at the equilibrium position[49] and subsequent filtering of the wave function with the lowest energy[50]. The energy of the ground state wave function was determined to be 0.233 eV above the minimal energy on the grid, which is in good agreement with the zero-point-energy derived from experimental vibrational frequencies using the harmonic-oscillator approximation (0.228 eV). The wave function was propagated with a split-step operator method[49], explicitly including the dipole-coupling of the two lowest-lying states due to the pump pulse[37]. The step size of a typical calculation was 0.02 fs. The wave functions were saved every 1 fs to serve as input for further calculations. The following approximations had to be made; first, the rotational motion of the molecules was not included. They were assumed to be aligned with their y-axis (cf. figure 1) along the polarization of the pump pulse. Second, the transition from the $^2A_1$ ground state to the $^2B_1$ second excited state was neglected. Previous work[51] showed this transition

to be weak compared to the transition to the $^2B_2$ state at excitation energies above 2.9 eV. Third, the Renner-Teller coupling of the $^2A_1$ with the $^2B_1$ state around $\theta = 0°$ and $\theta = 180°$ was not treated.

To depict the results of a propagation, we project the ground state vibronic wave function χ_0 out of the total wave function according to

$$\chi^{\mathrm{proj}}(t) = \chi(t) - \int_{\mathbf{R}} \chi_0 \chi(t)\, \mathrm{d}\mathbf{R} \chi(t)\,, \tag{7}$$

and calculate partial densities along specific coordinates with

$$\rho_r = \rho_{r_2} = \int \left|\chi_i^{\mathrm{proj}}(r, R, \theta)\right|^2 \sin\theta \; \mathrm{d}R\mathrm{d}\theta \tag{8}$$

$$\rho_\beta = \int \left|\chi_i^{\mathrm{proj}}(r_1, r_2, \beta)\right|^2 \frac{\sin\theta \; r_1}{R} \mathrm{d}r_1 \mathrm{d}r_2, \tag{9}$$

where χ_i^{proj} denotes the vibrational wave function of state i without contributions of the initial state.

C. Calculation of photoelectron spectra

Due to the number of the involved cationic states as well as their complexity, it was not possible to calculate the photoelectron spectra by direct propagation of the wave functions on the ionic surfaces[38]. Instead, we turned to a semiclassical model. The cross section σ for a transition at the energy E_{tr} can generally be written as

$$\sigma(E_{\mathrm{tr}}) = \frac{\pi e^2 E_{\mathrm{tr}}}{3\epsilon_0 c} \sum_{a,b} P_a |\langle \Psi_b | \, \hat{\mathbf{r}} \, | \Psi_a \rangle|^2 \delta(E_{\mathrm{tr}} - (E_b - E_a))\,, \tag{10}$$

where P_a is the population of the initial state, $\hat{\mathbf{r}}$ is the dipole operator, Ψ_a and Ψ_b are the initial and final molecular wave functions, respectively, and E_a and E_b are their energies[52]. Following the literature[53], one can express equation (10) in terms of the nuclear coordinates $\mathbf{R}$ and the electronic coordinates $\mathbf{r}$ by using the Born-Oppenheimer approximation as

$$\begin{aligned}\sigma(E_{\mathrm{tr}}) = C \sum_{i,k,f,l} P_{ik} \iint & \langle \psi_i(\mathbf{R}') \,|\, \hat{\mathbf{r}} \,|\, \psi_f(\mathbf{R}') \rangle \, \chi_{ik}^*(\mathbf{R}') \\ & \times \chi_{fl}(\mathbf{R}') \, \chi_{fl}^*(\mathbf{R}) \, \chi_{ik}(\mathbf{R}) \, \langle \psi_f(\mathbf{R}) \,|\, \hat{\mathbf{r}} \,|\, \psi_i(\mathbf{R}) \rangle \\ & \times \delta(E_{\mathrm{tr}} - (E_{fl} - E_{ik}))\, \mathrm{d}\mathbf{R}' \mathrm{d}\mathbf{R},\end{aligned} \tag{11}$$

where ψ_i and ψ_f are the initial and final electronic wave functions, respectively, χ_{ik} and χ_{fl} are the initial and final nuclear wave functions with their vibrational quantum numbers

collectively described by the indices k and l, and we collected the prefactors in C. Inserting the semiclassical approximation[54]

$$E_{fl} - E_{ik} \approx V_f(\mathbf{R}) - V_i(\mathbf{R})\,, \tag{12}$$

where V_i and V_f are the potential energies at coordinate $\mathbf{R}$ of the involved electronic states, and the identity

$$\sum_l \chi_{fl}(\mathbf{R}')\,\chi^*_{fl}(\mathbf{R}) = \delta(\mathbf{R}' - \mathbf{R}) \tag{13}$$

one obtains

$$\begin{aligned}\sigma(E_{\mathrm{tr}}) = C \sum_{i,k,f} P_{ik} \int &\left|\langle\psi_f(\mathbf{R})|\,\hat{\mathbf{r}}\,|\psi_i(\mathbf{R})\rangle\right|^2 \chi^*_{ik}(\mathbf{R}) \\ &\times\chi_{ik}(\mathbf{R})\,\delta(E_{\mathrm{tr}} - (V_f(\mathbf{R}) - V_i(\mathbf{R})))\,\mathrm{d}\mathbf{R}.\end{aligned} \tag{14}$$

This is known as the multidimensional reflection principle[55,56] without the kinetic energy correction[57,58], because the approximation in equation (12) neglects effects of the vibronic energy[53] and thus assumes that the kinetic energies of the nuclei do not change during the transition. As the electronic transition dipole moment $\mu_{if}(\mathbf{R}) = \langle\psi_f(\mathbf{R})|\,\hat{\mathbf{r}}\,|\psi_i(\mathbf{R})\rangle$ as well as the δ-function in equation (14) are independent of k, it can also be written in a time-dependent form

$$\begin{aligned}\sigma(E_{\mathrm{tr}}, t) &= C \sum_{i,f} \int |\mu_{if}(\mathbf{R})|^2\,\delta(E_{\mathrm{tr}} - (V_f(\mathbf{R}) - V_i(\mathbf{R}))) \\ &\quad\times \sum_k P_{ik}(t)\,\chi^*_{ik}(\mathbf{R})\,\chi_{ik}(\mathbf{R})\,\mathrm{d}\mathbf{R} \\ &= C \sum_{i,f} \int |\mu_{if}(\mathbf{R})|^2\,\delta(E_{\mathrm{tr}} - (V_f(\mathbf{R}) - V_i(\mathbf{R}))) \\ &\quad\times |\chi_i(\mathbf{R}, t)|^2\,\mathrm{d}\mathbf{R}.\end{aligned} \tag{15}$$

For simplicity, we contracted P_i into χ_i, such that

$$P_i(t) = \int |\chi_i(\mathbf{R}, t)|^2\,\mathrm{d}\mathbf{R}. \tag{16}$$

For photoionization, we define $V_f = E^{\mathrm{e}}_{\mathrm{kin}} + V_{\mathrm{cat},f}$, where $E^{\mathrm{e}}_{\mathrm{kin}}$ is the kinetic energy of the measured electron and $V_{\mathrm{cat},f}$ the electronic energy of the cationic state, to get

$$\begin{aligned}\sigma(E_{\mathrm{tr}}) = C \sum_{i,f} \int &|\mu_{if}(\mathbf{R})|^2\,|\chi_i(\mathbf{R}, t)|^2 \\ &\times \delta(E_{\mathrm{tr}} - E^{\mathrm{e}}_{\mathrm{kin}} - V_{\mathrm{cat},f}(\mathbf{R}) + V_i(\mathbf{R}))\,\mathrm{d}\mathbf{R}.\end{aligned} \tag{17}$$

As E_{tr} is typically constant in an experiment, we substitute it with the binding energy $E_{\mathrm{bind}} = E_{\mathrm{tr}} - E^{\mathrm{e}}_{\mathrm{kin}}$

$$\sigma(E_{\mathrm{bind}}) = C \sum_{i,f} \int |\mu_{if}(\mathbf{R})|^2 \, |\chi_i(\mathbf{R}, t)|^2 \times \delta(E_{\mathrm{bind}} - V_{\mathrm{cat},f}(\mathbf{R}) + V_i(\mathbf{R})) \, \mathrm{d}\mathbf{R}. \tag{18}$$

Because we did not diabatize the cationic potential energy surfaces, the adiabatic representation of χ_i, $V_{\mathrm{cat},f}$, and V_i is used to evaluate equation (18). As the electronic structure of the involved states is changing in this representation, $|\mu_{if}|^2$ is strongly configuration dependent. We approximate the dipole matrix element as the norm of the Dyson orbital[59–61] by using the sudden approximation, i.e. we disregard any continuum effects. The norm was determined by calculating a three-state-averaged CASSCF(13,10) CI-expansion of the lowest lying $^2\mathrm{A}'$ states of the neutral molecule with the aug-cc-pVQZ basis set, with a subsequent optimization of the CI-coefficients of all relevant states of the cation with invariant molecular orbitals. See appendix D for more details. In figure 3, the behavior of $|\mu_{if}|^2$ for a cut along θ is shown.

Using this approximation and defining the local ionization potential $I_p^{if}(\mathbf{R}) = V_{\mathrm{cat},f}(\mathbf{R}) - V_i(\mathbf{R})$, the photoelectron spectrum is given by

$$\sigma(E_{\mathrm{bind}}, t) = C \sum_{i,f} \int |\chi_i(\mathbf{R}, t)|^2 \, |\mu_{if}(\mathbf{R})|^2 \times \delta\big(E_{\mathrm{bind}} - I_p^{if}(\mathbf{R})\big) \, \mathrm{d}\mathbf{R}. \tag{19}$$

The cationic potential energies were shifted collectively by 0.32 eV in order to maximally overlap the photoelectron bands with the experimental spectrum of NO_2. Using the calculated time-dependent wave functions, photoelectron spectra of individual channels can be calculated according to equation (19).

Depending on the excitation energy, a significant part of the wave function runs into the absorption barrier at large R and r. To include the absorbed population into our model, its spectrum σ_{abs} has to be approximated. To take the configuration dependence of the spectra of the absorbed parts of the wave functions into account, we calculated the time-integrated density

$$P_{\mathrm{int}}(r, R, \theta) = \int_t \left|\chi^{\mathrm{proj}}(r, R, \theta, t)\right|^2 \mathrm{d}t \tag{20}$$

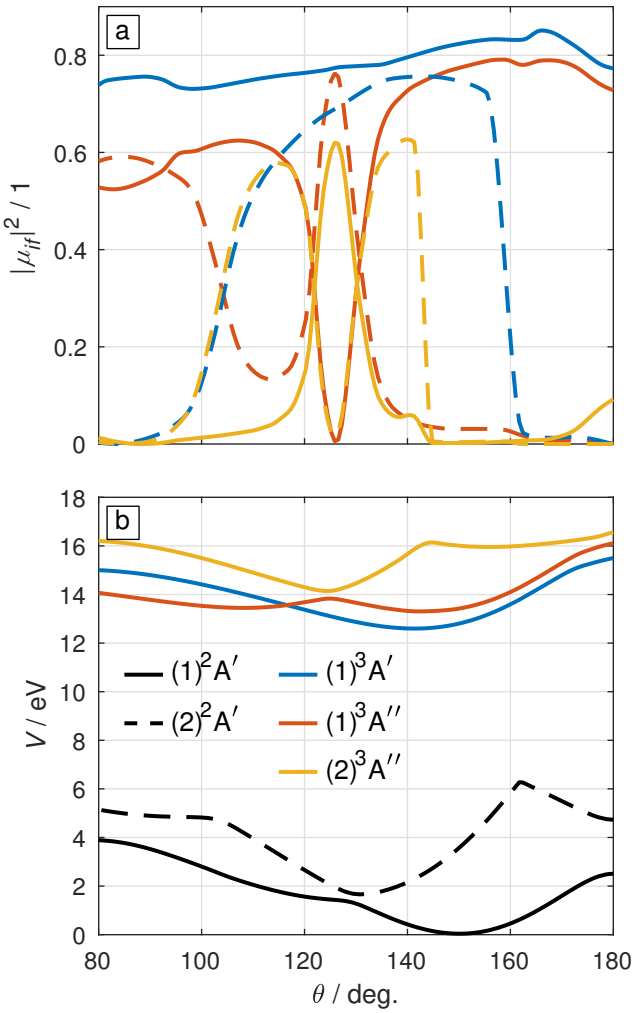

FIG. 3. Illustration of the calculated transition-matrix element $|\mu_{if}(\mathbf{R})|^2$ for the example of the transitions from the two energetically lowest adiabatic ^{2}A′ states (black curves in (b)) to the cationic $(1)^3$A′ (blue), $(1)^3$A″ (red) and $(2)^3$A″ (yellow) states in a cut through $r = 1.1625$ Å and $R = 1.7047$ Å. (a) Dyson norm. The color indicates the final state and the line style the initial state. (The legend is given in the lower panel.) (b) Cut through the potential surfaces of the states. The magnitude of the overlap is strongly dependent on the electronic structure of the initial and the final state. Avoided crossings in the involved states can lead to sharp changes in the Dyson norm, as can be observed for the case of the transition from $(2)^2$A′ to $(2)^3$A″ (dashed yellow line) due to the crossing at $\theta = 140°$ in the final state. However, not all crossings lead to a change in Dyson norm, as can be observed for the crossing of the neutral states at $\theta = 130°$ in the transition to the $(1)^3$A′ state (solid blue line).

and from this the conditional probability density in r

$$P_{\mathrm{cond}}(R,\theta\,|r\,) = \frac{P_{\mathrm{int}}(r,R,\theta)}{\int_{R,\theta} P_{\mathrm{int}}(r,R,\theta)\sin\theta \mathrm{d}R\mathrm{d}\theta}. \tag{21}$$

The photoelectron signal of the absorbed wave packet can then be approximated by

$$\begin{aligned}\sigma^{if}_{\mathrm{abs}} = C \int_{\mathbf{R},r\geq r_{\mathrm{abs}}} & P_{\mathrm{cond}}(\mathbf{R})\,|\mu_{if}(\mathbf{R})|^2 \\ & \times\delta\big(E_{\mathrm{bind}} - I_p^{if}(\mathbf{R})\big)\,\mathrm{d}\mathbf{R}.\end{aligned} \tag{22}$$

The total photoelectron signal was then calculated using

$$\begin{aligned}\sigma^{\mathrm{tot}} &= \sum_{i,f} \sigma^{if}(E_{\mathrm{bind}},t) \\ &= \sum_{i,f} \sigma_0^{if}(E_{\mathrm{bind}},t) + (1-P(t))\,\sigma^{if}_{\mathrm{abs}}(E_{\mathrm{bind}},t)\,,\end{aligned} \tag{23}$$

where $\sigma_0^{if}(E_{\mathrm{bind}},t)$ is the photoelectron spectrum without absorbed contributions from state i to state f and P is the total population in the grid. We simulated the limited energy resolution of the experiment by convolving the resulting spectrum with a Gaussian with a FWHM of 0.35 eV. To simulate the probe pulse, the spectra were convolved with a Gaussian with a FWHM of 8 fs (electric field envelope).

III. RESULTS

A. Potential-energy surfaces

The potential-energy surfaces used in the propagation agree very well with earlier high-level calculations and experimental values (see table I). The dissociation threshold, which is shifted by -0.2 eV (-6.25 %) from the experimental value, shows the largest deviation. A cut through the calculated potential energy surfaces with $r_{\mathrm{NO}} = 1.625$ Å is shown in figure 4.

B. Vibronic wave packets

The result of a wave packet propagation with a Fourier-limited excitation pulse of 8 fs duration (FWHM of the electric field envelope), centered at 400 nm, and a peak intensity

TABLE I. Comparison of the calculated potential surface with Kurkal et al.[32] and experimental values.

	this work			Kurkal et al.[32]			Experiment		
	V / eV	$r_1 = r_2/a_0$	β/deg.	V / eV	$r_1 = r_2/a_0$	β/deg.	V / eV	$r_1 = r_2/a_0$	β/deg.
$(1)^2A_1$ minimum	0	2.258	134.0	0	2.2609	134.3	0	2.255[1]	133.9[2]
$(1)^2B_2$ minimum	1.248	2.380	101.9	1.31	2.3659	101.9	1.21[3]	2.351[3]	102.6[3]
$(1)^2\Pi_u$ minimum	1.766	2.266	180	1.726	2.263	180	1.83[4,5]	2.324[4,5]	180
$(1)^2A_1/(1)^2B_2$ cusp	1.313	2.374	107.4	1.28	2.3590	106.6	1.21±0.09[1]	2.355[1]	103.1[1]
$(1)^2A'$: NO + O	3.028			3.11			3.23[6,7]		

of $1 \cdot 10^{12}$ W/cm^2 is illustrated in figures 5 and 6. Figure 5 (Multimedia view) shows the density of the excited wave packets with isosurfaces. It is a static representation of the linked animation of the densities in steps of 1 fs. Figure 6 shows the partial densities in r and β as defined in the equations (8) and (9) and the behavior of the populations in the electronic states. Note that the partial density in r has to remain in the C_{2v} symmetry of the vibronic ground state equilibrium of the molecule, i.e. $\rho_r = \rho_{r_2} = \rho_{r_1}$. Thus, a molecule which is strongly asymmetrically stretched is associated with density at small and large r at the same time.

The excited wave packet initially moves symmetrically towards longer r_1 and r_2 and smaller β and reaches the conical intersection within 12 fs after its excitation, where most of the population transfers to the lower adiabatic state. The remaining part of the wave packet scatters at the conical intersection and reaches a turning point at $\theta \approx 100°$ and 14 fs, moving back towards the conical intersection (cf. the upper panels of the figures 5a-d and 6b). The excited wave packet on the lower adiabatic state reaches the turning point at $\beta \approx 88°$ later (20 fs) and afterwards moves towards 180° (lower panels). In contrast to this, the turning point in r occurs earlier (16 fs), leading to a maximal contraction of the molecule (around 24 fs), and a subsequent expansion (fig. 6a, bottom). Only during this extension is the asymmetric stretch mode significantly excited, where one NO bond length oscillates around the equilibrium distance, while the other oxygen moves towards the absorption barrier (at 3.0263 Å). Simultaneously, the wave packet spreads in the angle dimension. The leading edge of the wave packet reaches the absorbing barrier after 87 fs (figures 5g-j and 6). The

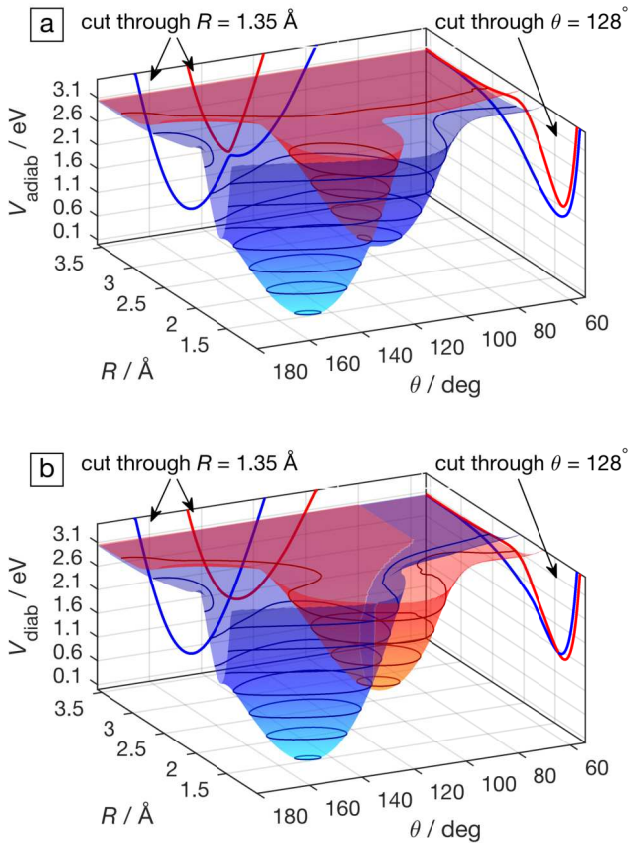

FIG. 4. Cut at $r = 1.625$ Å through the $^2A'$ potential energy surfaces of neutral NO_2 in Jacobi coordinates. The top panel (a) shows the adiabatic potentials, the result of the diabatization is shown in the lower panel (b). In the back planes, a cut thorugh $R = 1.35$ Å is shown, and on the right, cuts through $\theta = 128°$ are illustrated.

second crossing of the upper adiabatic wave packet over the conical intersection around 20 fs after the excitation (fig. 5b-d) leads to a second distinct wave packet on the lower surface, which does not lead to fast dissociation. While the coherent vibration of one of the bond lengths is visible until the end of the simulation (fig. 6a), the wave packet clearly disperses very rapidly, such that no distinct variations in the wave-packet density can be observed for times longer than ∼150 fs. The loss of population due to absorption is mainly caused by the elongation of the bond length into the absorbing barrier at large r, rather than at small β.

The chosen pump pulse excites 2.58 % of the sample. The adiabatic population dynamics show that most of the excited population relaxes to the adiabatic ground state with the first crossing of the conical intersection. The significant net transfer to the upper adiabatic state

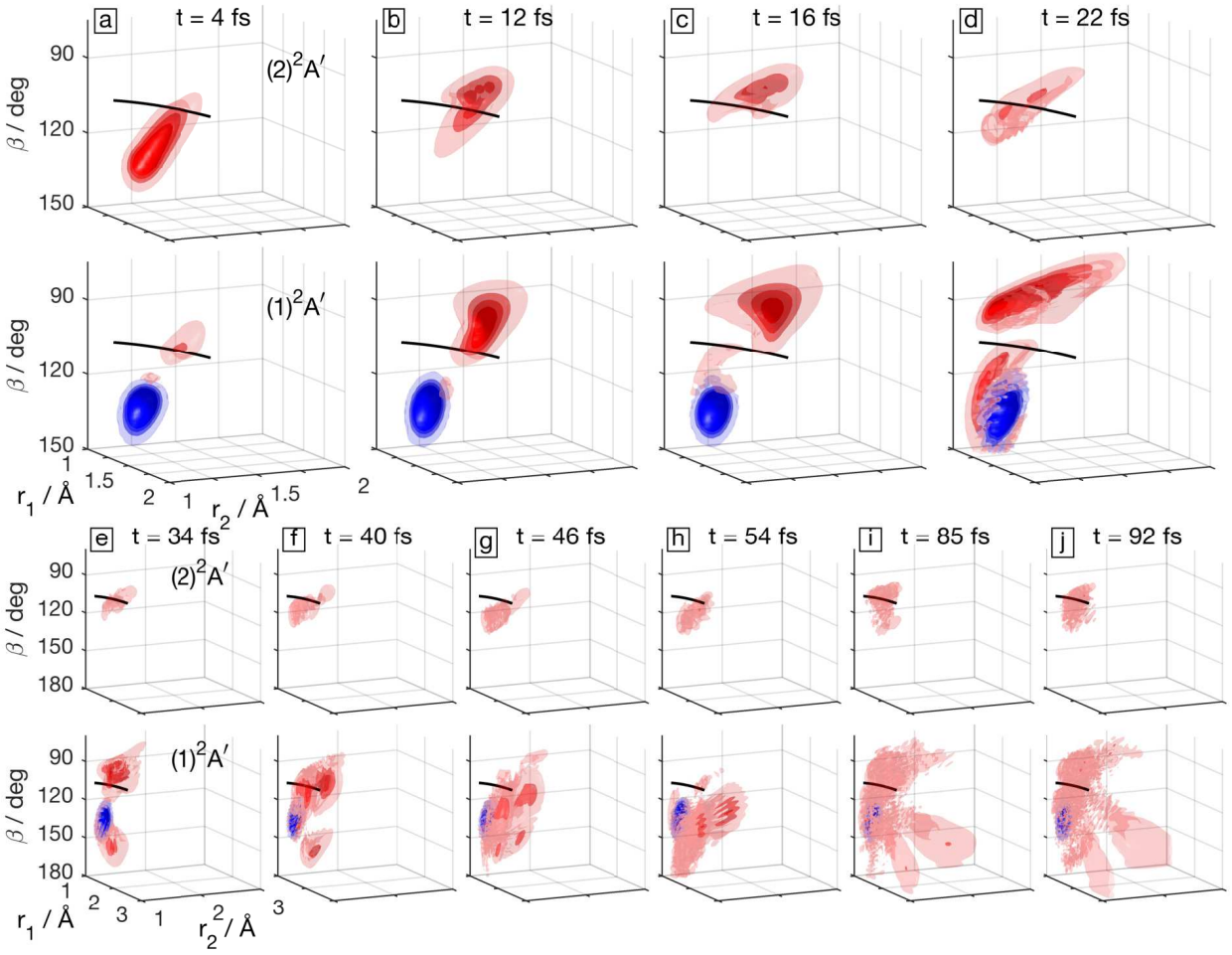

FIG. 5. Isosurfaces of the time-dependent difference in adiabatic nuclear densities in internal coordinates calculated as $\rho_i(t) = |\Psi_i(t, \mathbf{R})|^2 - |\Psi_i(t = 0, \mathbf{R})|^2$. Blue are negative contributions, i.e. where population was removed due to the excitation, and red are positive contributions. The black line indicates the seam of the conical intersection. Linked is animated version of this figure in steps of 1 fs (Multimedia view). An animation of the isosurfaces shown from another perspective is part of the supplementary material.

around 38 fs correlates with the second crossing of the initially formed wave packet across the conical intersection, visible in fig. 5e-f and 6b.

The results of our new calculations closely resemble the original work over the first 50-100 fs, i.e. before the wave packet has started to explore the dissociative regions of the potential energy surface. This can be seen by comparing the population dynamics shown in fig. 6c of the present article with fig. 3 of ref. 37. The population dynamics for longer delays are also similar, i.e. the population of the upper diabatic state (red curve in fig. 6c) shows local

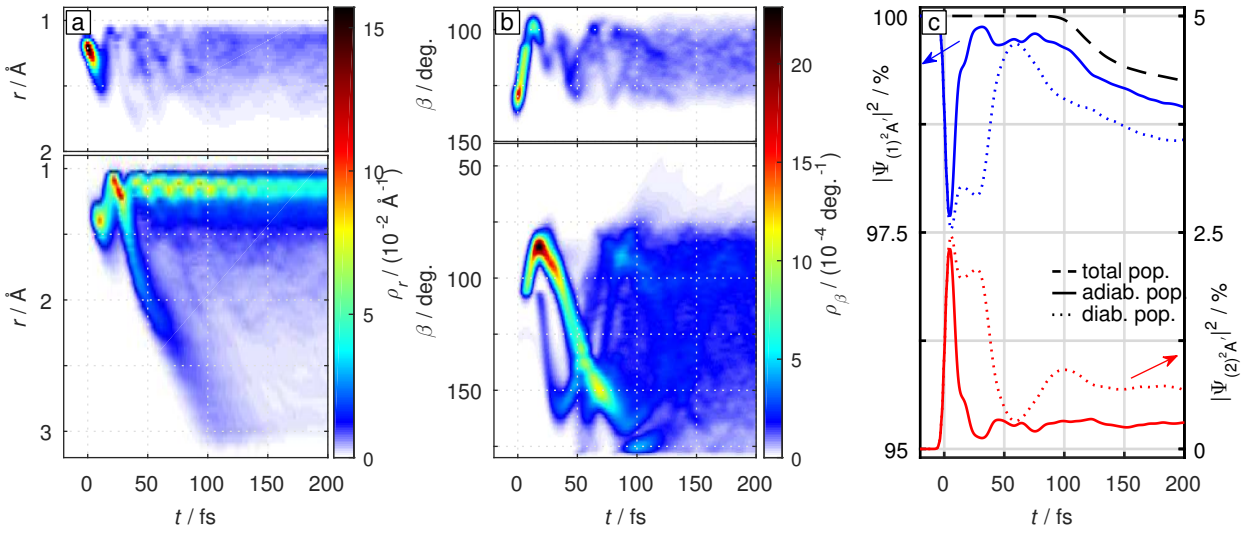

FIG. 6. Results of a wave packet calculation with an 8-fs long excitation pulse (see text for details). (a) Adiabatic projected densities ρ_r for the $(2)^2\mathrm{A}'_\mathrm{A}$ and $(1)^2\mathrm{A}'_\mathrm{A}$ states in the upper and lower panel, respectively. (b) Adiabatic projected densities ρ_β. (c) Populations: dotted lines represent the diabatic representation and solid lines the adiabatic representation. The total population in the grid is shown with the black dashed curve (left scale).

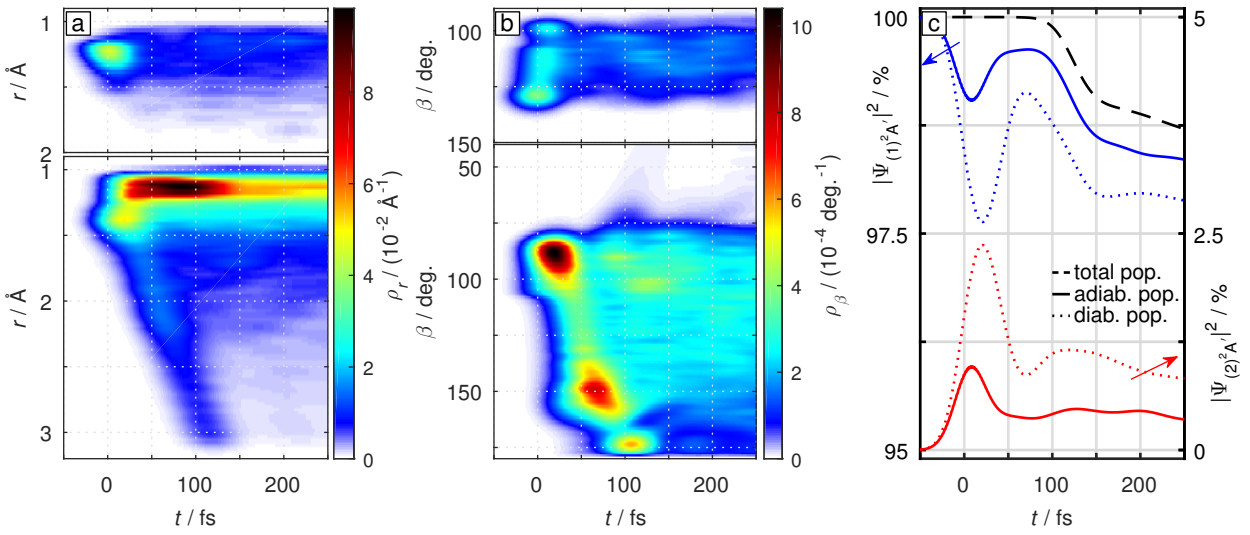

FIG. 7. Result of a wave packet calculation with a 56 fs long excitation pulse. (a) Adiabatic projected densities ρ_r for the $(2)^2\mathrm{A}'_\mathrm{A}$ and $(1)^2\mathrm{A}'_\mathrm{A}$ states in the upper and lower panel, respectively. (b) Adiabatic projected densities ρ_β. (c) Populations: dotted lines represent the diabatic representation and solid lines the adiabatic representation. The total population in the grid is shown with the black dashed curve (left scale).

maxima at 100 and 170 fs in both calculations. However, the local maxima are somewhat less pronounced in the new calculations compared to ref. 37.

Experimentally, pump pulses of 8 fs are difficult to achieve and very challenging to apply to single-photon excitation. The total excitation fraction indeed scales with the total pump fluence, whereas multi-photon excitation and ionization scale faster than linearly with the peak intensity. Therefore, it is challenging to achieve a sufficient excitation fraction (e.g. > 1 %), while avoiding multi-photon processes with a short pump pulse. Recent experimental work[24] therefore used 56 fs long (FWHM of the electric field envelope, i.e. 40 fs FWHM of the intensity envelope) excitation pulses. The longer excitation duration leads to a significant broadening of the wave packets in configuration space, as can be seen in figure 7. In particular, the longer pump pulse blurs the fine details of the fast wave-packet motion in the bond-length coordinate, especially the predicted coherent vibrations in the lower adiabatic state (fig. 6a). The slower dynamics in the bond-angle coordinate are less affected by the long pump pulse. In this case, the dominant part of the wave packet moving to larger bond angles on the lower adiabatic surface is preserved (fig. 7b). The main difference between the dynamics induced by the short and long pulses is the blurring of the second wave-packet component created on the lower adiabatic surface around t=20 fs when the conical intersection is approached for the second time. However, the relative amplitude of this second wave packet component is small in fig. 6b, explaining why the dominant features observed in the case of the 8-fs pulse are retained in the case of the 56-fs pulse. A similar conclusion is reached when comparing the population dynamics in figs. 6c and 7c. The main features in the population dynamics induced by the long pump pulse can be rationalized as a temporal convolution of the short-pulse dynamics with a Gaussian envelope.

In the picosecond time range, the dynamics are known to be complex. Individual resonances show strongly varying dissociation constants close to the dissociation threshold, leading to excitation-energy-dependent dissociation times[62,63]. In picosecond and femtosecond time-resolved experiments, due to the bandwidth of the excitation pulse and the associated spectral averaging, a monotonic increase of the dissociation rates with increasing excitation energies[64,65] has been reported (see crosses in fig. 8b). This trend is reproduced by our calculations. Figure 8a shows the adiabatic and total populations as a function of time for different excitation energies. For all excitation energies, we observe an initial fast

decay due to the coherent movement of a wave packet to the absorption barrier around 150 fs after excitation. Subsequently, the dissociation can be approximated by an exponential decay. The extracted dissociation times τ, which are determined by exponential fits to the total population at 250 fs $< t <$ 10 ps are shown as black circles in fig. 8a. These results cannot directly be compared with the experimental dissociation rates, because the latter were obtained with picosecond pump pulses with correspondingly narrower spectra. We have therefore converted the decay rates from the literature (crosses) into expected decay rates induced by 56-fs pulses as described in Appendix E. The result is displayed as a red line in fig. 8b. Our calculations reproduce the general trend of an increasing dissociation rate with increasing excess energy and agree with the experimental results for excess energies above 0.1 eV. Our calculations overestimate the dissociation rate at lower excess energies, and in particular for the cases where the spectrum of the pump pulse is centered below the dissociation threshold.

C. Photoelectron spectra

The time-dependent wave functions can be used to calculate extreme-ultraviolet time-resolved photoelectron spectra[24,66] according to equation 23. The time-dependent spectrum of NO_2, assuming an 8-fs long pump pulse centered at 400 nm and an 8-fs long probe pulse centered at 45.75 nm (27.1 eV) with a bandwidth of 0.33 eV, is depicted in fig. 9a. In this article, we concentrate on the analysis of the time-dependent photoelectron spectra generated by these short pulses. The comparison of calculations with longer pulses and experimental data will be shown in a future publication[24]. We consider all transitions from the neutral $(1)^2A'$ and $(2)^2A'$ states to each of the energetically lowest-lying two states of $^1A'$,$^1A''$,$^3A'$, and $^3A''$ character of the cationic molecule. The spatially confined character of the wave packets up to 70 fs after excitation leads to strong modulations in the spectrum. For delays larger that 70 fs, i.e. when the wave packet covers a dominant fraction of the available configuration space and one NO-bond is significantly elongated, the spectrum can be structured into three parts: ionization of the NO-fragment leading to a band around 9.3 eV, ionization of the O-fragment leading to a sharp band around 13.3 eV, and the hot ground state of NO_2 leading to a broad band ranging from 10 to 14 eV, peaking at 12.3 eV. Note that significant loss of population in the grid only occurs for delays longer

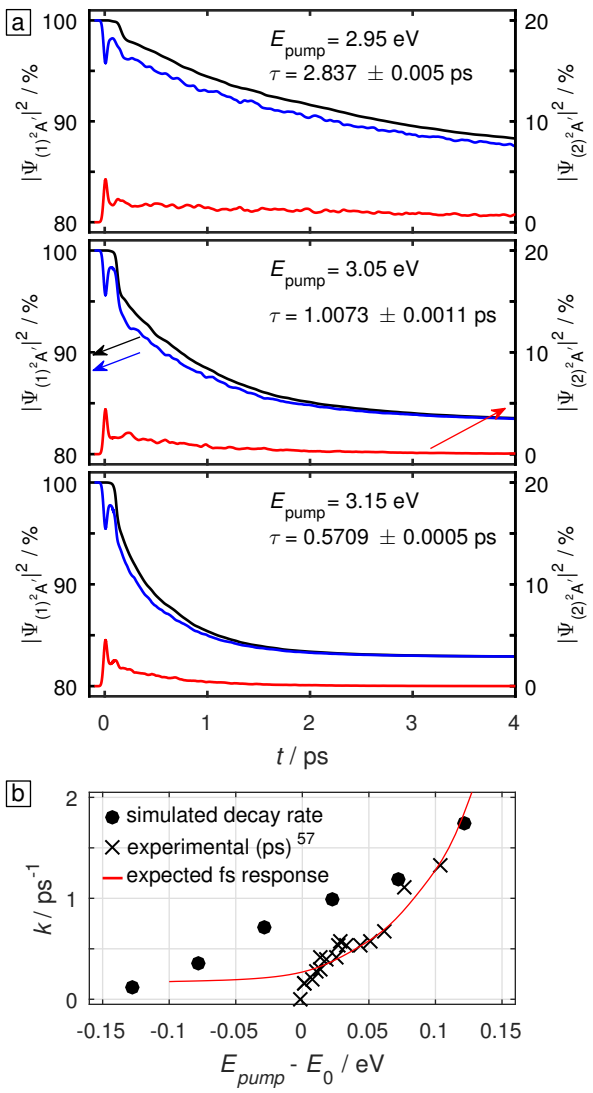

FIG. 8. Simulation of the picosecond dissociation dynamics of NO_2: Results of wave packet calculations with a 56 fs long excitation pulse centered at 2.95, 3.05 and 3.15 eV with a peak intensity of $1 \cdot 10^{12}$ W/cm^2 in the top, middle and bottom panel, respectively. The total population (black) and the population of the lower adiabatic state (blue) are indicated with the left scale, the population of the upper adiabatic state (red) is indicated with the right scale. The parameter τ is the lifetime of the excited molecule determined by a fit to $P_{\mathrm{tot}} = a \exp(-t/\tau) + b$ with $t \in [0.25, 10]$ ps. (b) Decay constants vs. energy offset of the central pump energy E_{pump} with respect to the calculated dissociation energy $E_0 = 3.028$ eV. The expected experimental femtosecond response of the system was simulated with an exponential fit to the population when exciting with a Fourier-limited laser pulse characterized by a gaussian spectrum centered at the pump energy[63]. Experimental values were taken from picosecond time-resolved measurements[64].

than 100 fs (cf. figure 6). To illustrate the accuracy of the method, fig. 9b compares the calculated spectrum of unexcited NO_2 to the correpsonding experimental spectra. The blue line shows the experimental spectrum reported by Baltzer et al.[8] using He-I radiation (21.2 eV), whereas the red line shows experimental spectrum obtained in our laboratory using a 27.1 eV high-harmonic source[24]. The yellow line shows the calculated photoelectron spectrum with all photoionization matrix elements μ_{if} set to unity, whereas the black line shows the full calculation that uses the Dyson norm as an approximation to these matrix elements. A good agreement is obtained between the full calculation and our experimental spectrum. In particular the relative intensities are all reasonably well reproduced, the largest deviation (of less than a factor of two) occurring for the band at 13.0 eV binding energy, i.e. the $(1)^3B_2$ ($(1)^3A'$) state of NO_2^+. This agreement motivates our use of the Dyson-norm approximation in the present work. The comparison of the experimental results further shows the significant variation of the photoionization cross section into the $(1)^3B_2$ ($(1)^3A'$) continuum as a function of the photon energy. The comparison of the two calculations further shows the importance of including the photoionization matrix elements as the latter entirely suppress the broad photoelectron band centered around 16 eV because the corresponding photoionizing transitions are forbidden by Koopman's correlations. The absence of the photoelectron band with an onset at ∼17 eV from both calculations is due to the fact that the corresponding states of the cation ($(3)^3A'$ and $(3)^3A''$ according to ref. 8) were not included in our calculation.

These calculations reveal the complex nature of the time-dependent photoelectron spectra of the excited-state dynamics in NO_2. The present calculations are therefore essential for a detailed interpretation of experimental XUV-TRPES spectra, because they enable an identification of the contributions of individual channels. The contributions of the different channels are exemplarily shown for a pump-probe delay of 50 fs in 9c.

Figure 10 shows the signal arising from the ionization channel from the coupled states of the neutral molecule to the $(1)^1A'$ state of the cation in more detail. While the binding energy of the photoelectron is determined by the local ionization potential I_p at the position of the wave packet, the probability to ionize is determined by the photoionization matrix element. Cuts through the potential surfaces along r and β are illustrated in the figure 10a, which give rise to the I_p shown in panel b. The electronic structures of the states lead to a strongly varying matrix element along these cuts (panel b, right scale). A calculation

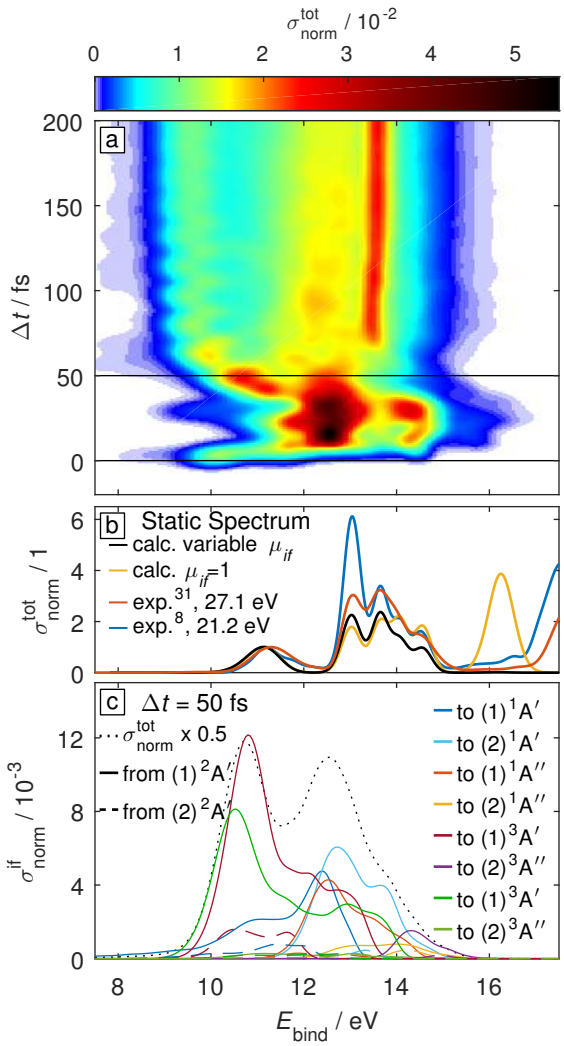

FIG. 9. Calculated time-dependent photoelectron spectrum of NO_2. (a) Total time-dependent photoelectron spectrum of the excited part of the wave function. (b) Comparison of the static spectrum calculated from the ground-state wave function with experimental spectra (red[24] and blue[8]). The calculation using a constant photoionization matrix element μ_{if} (yellow) shows a significantly worse agreement with the experiment than the calculation including variable matrix elements (violet). (c) Individual contributions from different channels to the photoelectron spectrum at a pump-probe delay Δt of 50 fs. The contributions from different channels are differentiated by their initial states (solid and dashed) and final states (colors). All spectra are normalized with respect to the maximum of the cross-section of the first photoelectron peak (assigned to the transition $(1)^2A_1 \rightarrow (1)^1A_1$ around $E_{bind} = 11.2$ eV) of the static spectrum.

with the transition matrix elements set to 1, as illustrated in panel c, shows the strong modulations due to the movement of the wave packet. For example, the excitation in the Franck-Condon region leads to the appearance of a peak at 8.1 eV, which is offset from the binding energy of the corresponding band in the static photoelectron spectrum by the excitation energy. The peak is shifting fast towards higher binding energies as the wave packet moves towards the conical intersection (mainly along β). The crossing of the conical intersection leads to the appearance of the transition from the lower adiabatic state, which initially shows strong modulations due to the oscillation in β and r (see figure 6). The intensity maximizes due to accumulation of density at turning points of the dynamics or, on longer time scales, when the wave packet reaches areas where the local I_p is similar for many configurations (e.g. when the molecule reaches configurations with an elongated r). The spread of the wave packet in the potential leads to a spectrum with 4 eV width. If one includes the ionization probability (fig. 10d), the direct interpretation of the spectra becomes more complicated. Exemplarily, the ionization of the initially formed wave packet is strongly suppressed, leading to the near-vanishing of the expected peak at 8.1 eV around $\Delta t = 0$. In the case of the transition to the $(1)^1\mathrm{A}'$ state, the ionization of the NO fragment is Koopman's forbidden, such that the band is losing intensity when the molecule reaches strongly stretched configurations. The large range of local I_ps covered by the wave packet, which leads to the overlap of contributions from many ionization channels, as well as the strong influence of the matrix element, make it challenging to interpret experimental time-resolved photoelectron spectra without extended theoretical modeling of the system[24,66].

IV. CONCLUSION

The potential energy surfaces presented here are, to our knowledge, the most spatially extended (for NO_2^+) and are obtained at the highest level of theory (for NO_2) published so far. We performed full-dimensional wave-packet calculations on the electronic surfaces of the neutral molecule, revealing the signatures of the conical intersection and extending the time scale of previous studies to the picosecond range. This enabled us to report time-dependent photoelectron spectra for a broad range of binding energies and involving many ionization channels which are needed for a direct comparison to recent experimental results in XUV time-dependent photoelectron spectroscopy (XUV-TRPES)[24]. The comparison allows for a

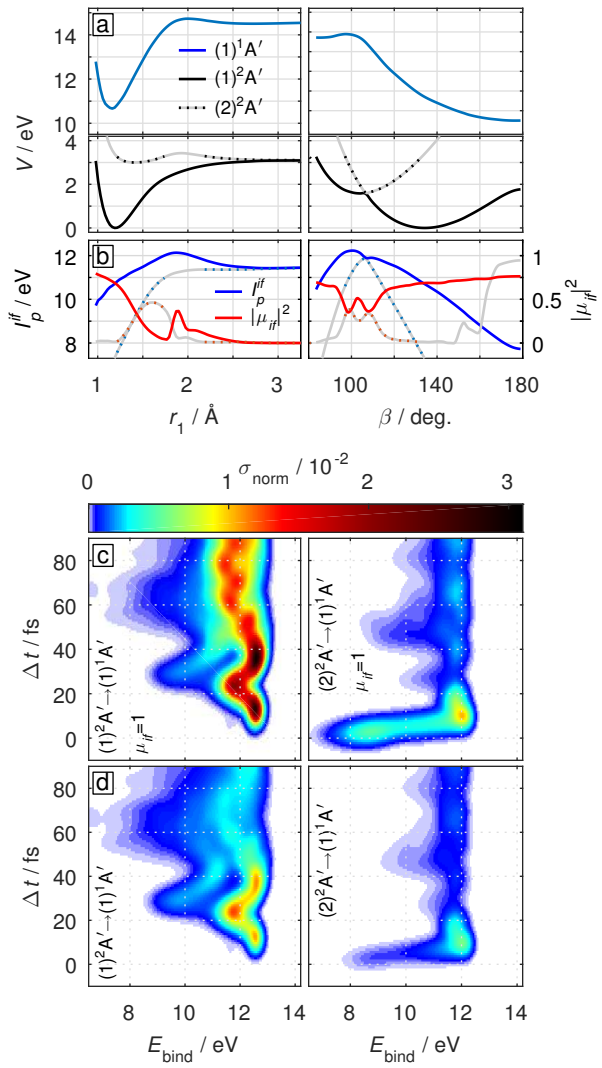

FIG. 10. Illustration of the photoionization channels $(1)^2\mathrm{A}' \rightarrow (1)^1\mathrm{A}'$ and $(2)^2\mathrm{A}' \rightarrow (1)^1\mathrm{A}'$. (a) shows the potential surfaces of the involved states in cuts along r_1 with $r_2 = 1.190$ Å and $\beta = 134°$ (left) and β with $r_1 = r_2 = 1.190$ Å(right). The potentials of the neutral molecule are only shown in regions which are energetically accessible to the wave packet. Both, the ionization potentials depicted in (b) (left scale, blue), as well as the norm of the Dyson orbital (red, right scale) vary strongly along the cuts. Panel (c) depicts the calculated photoelectron spectrum of the channels with the matrix elements set to 1, while panel d illustrates the complete implementation of equation 19.

stringent test of the ab-initio method presented here. The calculations allow interpretations of time-dependent spectra of XUV-TRPES, laying the foundation for a quantitative evaluation of such experiments. They also open the perspective for the quantitative interpretation of time-resolved high-harmonic spectroscopy and several other experimental techniques, such as core-level transient absorption spectroscopy[67] by using similar techniques. Finally, NO_2 is an ideal candidate to demonstrate electronic control over non-adiabatic wave-packet dynamics[68–70], one of the major perspectives of attosecond science.

SUPPLEMENTARY MATERIAL

The Supplementary Material available with this article consists of the following files:

- NO2_2Ap.txt: Adiabatic and diabatic energies of the doublet A′ states of NO_2. Table of potential energies and dipole moments along the y-axis of the two energetically lowest lying doublet A′ states of the neutral NO_2 molecule in dependence of the Jacobi coordinates. The table is organized in 14 columns and has one header row. The first three columns are the indices i_r, i_R and i_θ according to equations (1) to (3) in the main text of the article. The columns 4 to 6 are the associated Jacobi coordinates r, R, and θ. The distances are given in Angstrom, the angle in degrees. The subsequent two columns, 7 and 8, are the calculated adiabatic energies in eV of the $(1)^2$A′ and $(2)^2$A′ states, respectively. Columns 9 and 10 describe the diabatic potential energies in electron Volts. Column 11 is the coupling matrix element between the two surfaces in eV. The columns 12 and 13 are the dipole moments along the y-axis of the two states in debye. Column 14 is the transition dipole along the y-axis between the states in debye. The dipole moments are direct outputs of the Molpro program. The sign of the transition dipole moment is adjusted to correct for the arbitrary phase-flipping in the calculation. The axis convention is given in figure 1 of the article.

- NO2_1Ap.txt: Adiabatic energies of the singlet A′ states of NO_2^+. Table of the adiabatic potential energies of the two energetically lowest lying singlet A′ states of NO_2^+ in dependence of Jacobi coordinates. The table is organized in 8 columns and has one header row. The first five columns contain the same information as in the paragraph above. The subsequent two columns, 7 and 8, are the calculated adiabatic energies in

eV of the $(1)^1A'$ and $(2)^1A'$ states, respectively.

- NO2_1App.txt: Adiabatic energies of the singlet A″ states of NO_2^+. Same as previous item for the two energetically lowest lying singlet A″ states of NO_2^+.

- NO2_3Ap.txt: Adiabatic energies of the triplet A′ states of NO_2^+. Same as previous item for the two energetically lowest lying triplet A′ states of NO_2^+.

- NO2_3App.txt: Adiabatic energies of the triplet A″ states of NO_2^+. Same as previous item for the two energetically lowest lying triplet A″ states of NO_2^+.

- WP8fs_r_200fs.avi: An animation of the time-dependent wave-packet dynamics viewed from a different perspective compared to Fig. 5.

ACKNOWLEDGMENTS

This research was funded in parts by the European Research Council under the European Unions Seventh Framework Programme (FP/2007- 2013)/ERC Grant Agreement No. 307270-ATTOSCOPE, the National Centre of Competence in Research Molecular Ultrafast Science and Technology (NCCR-MUST), a research instrument of the Swiss National Science Foundation (SNSF), as well as a Grant-in-Aid for Basic Science from the ministry of Education and Science of Japan (15H05752).

Appendix A: Potential surface calculations

For the calculation of the potential energy surfaces of the neutral molecule, two main difficulties had to be treated. First, as can be seen in fig. 11, a sharp avoided crossing of the second with the third $^2A'$ state at large θ and r below 1.5 Å led to an artificial jump in the calculated energy of the lower state (indicated by an arrow). This was corrected by calculating the relevant volume without state-averaging, and shifting the energy to maximize the overlap at smaller θ. As the energy of the $(2)^2A'$ state is larger than 4 eV and the diabatic coupling of the lowest two states is negligible, no accurate energy of the higher state is needed at these structures.

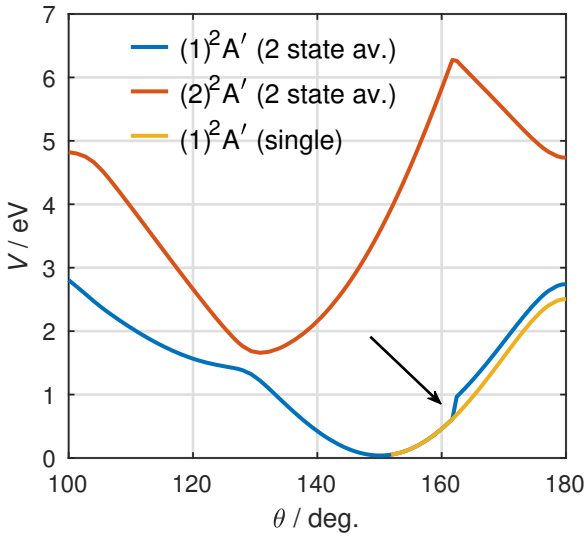

FIG. 11. Illustration of the artifact at large θ and small r in the adiabatic potentials: Blue and red: state-averaged potential surfaces. Yellow: single state calculation of the lower surface, shifted for minimal deviation between 152 and 161 degrees.

Second, due to the approximation of the $(3)^2\mathrm{A}'$ state to the lower states at large R, three-state averaged calculations had to be performed in these regions. The energy was shifted for minimal deviation along $R = 3.1469$ Å.

Appendix B: Diabatization details

For $r > r_{\mathrm{ref}} = 1.8188$ Å, the third $^2\mathrm{A}'$ state couples too strongly to the other states to use the phenomenological diabatization method. Instead, the angle was taken to be constant (i.e. $\alpha_{\mathrm{D}}(\theta, R, r > r_{\mathrm{ref}}) = \alpha_{\mathrm{D}}(\theta, R, r = r_{\mathrm{ref}})$), which was checked by comparing to cuts at larger r. An example is shown in fig. 12. For large R, the same problem occurred. Here, the construction of the diabatic potentials was more involved. We used an inherent property of the Jacobi coordinates; for every set of Jacobi-coordinates (θ, R, r), there is a second set

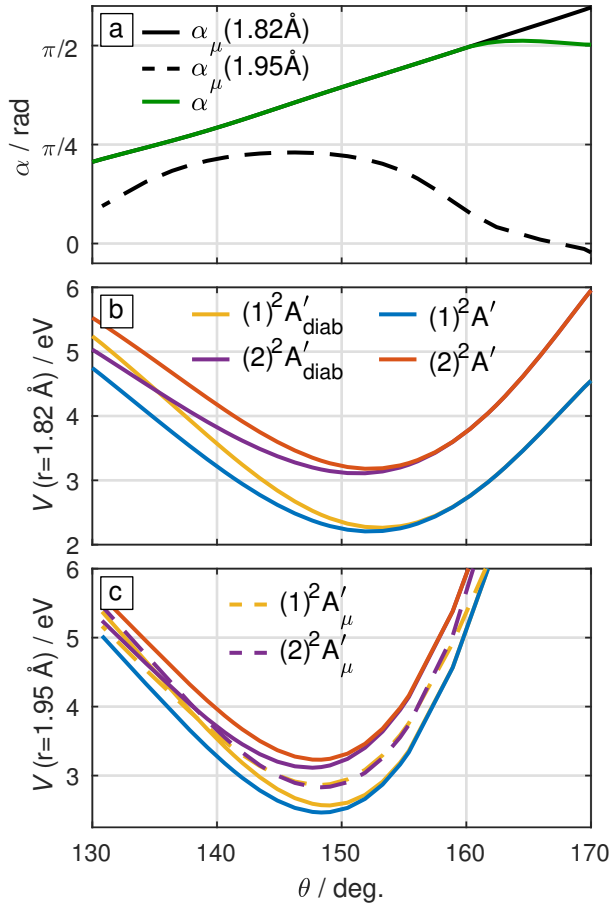

FIG. 12. Illustration of the diabatization process at long r. Shown are cuts through the hypersufaces with $R = 1.9266$ Å and with $r = r_{\text{ref}} = 1.8188$ Å and $r = r_1 = 1.9500$ Å, respectively . (a) Mixing angles: The black curve shows the mixing angle calculated from the dipole moments at $r = r_{\text{ref}}$ (according to eq. 4) and the green curve its modification for the diabatization procedure. The black dashed curve illustrates the calculated diabatization angle for $r = r_1$. (b) Potential surfaces for $r = r_{\text{ref}}$: the adiabatic potentials in red and blue, the diabatic potentials in yellow and violet. (c) Potential surfaces for $r = r_1$: same color code as in (b). Additionally, the dashed curves indicate the diabatic surfaces calculated with the dipole-dependent mixing angle α_μ (shown as the black dashed curve in panel a). The proximity of the third adiabatic state leads to problems with the phenomenological model of the diabatization. The mixing angle was approximated by the values at $r = r_{\text{ref}}$.

(θ', R', r') with identical properties, where

$$r' = \sqrt{\left(mr + R\cos\theta\right)^2 + R^2\sin\theta^2}, \tag{B1}$$

$$R' = \sqrt{m^2R^2 + 2m\left(m^2-1\right)rR\cos\theta + \left(m^2-1\right)^2 r^2}, \tag{B2}$$

$$\theta' = \mathrm{atan2}\left(\frac{rR\sin\theta}{mr^2 - m^3r^2 - mR^2 + (1-2m^2)rR\cos\theta}\right), \tag{B3}$$

$$m = \frac{m_\mathrm{O}}{m_\mathrm{O} + m_\mathrm{N}}. \tag{B4}$$

Here, m_O and m_N are the atomic masses of O and N. The diabatic potentials around (θ', R', r') were used to interpolate the potential and extract a mixing angle for (θ, R, r). For a set of coordinates with 2.0375 Å $\leq R \leq$ 2.2594 Å, this enabled us to make an educated guess how to consistently extrapolate the mixing angle into areas (at small θ) where three states interact. Further out, with $R >$ 2.2594 Å, the interpolated mixing angles were fitted with a heuristic function $\alpha = a\ \arctan(b\ \theta + c) + \pi/4$ for each cut along θ.

Appendix C: Interpolation

The adiabatic and diabatic energies, as well as the dipole moments at the calculated points were interpolated on the complete grid by iterative one-dimensional Akima-interpolations[71]. Sections of the surface with at least six subsequent points with a maximal distance of d between them were searched and the missing points in between them interpolated (only interpolating up to the third point from each end of the array). The new set of points was included in the similar next interpolation along the second dimension (R). This was repeated along the first two dimensions with increasing d. Then, the interpolation along the third dimension (r) was performed and the process repeated until no additional points were generated anymore. Finally, the interpolation was extended to the data points at the edge. For the interpolation along θ, the mirror plane at $\theta = 180°$ was taken into account. As the interpolations of the diabatic and adiabatic surfaces were performed independently, small errors had to be corrected afterwards: e.g., if the lowest diabatic energy at a certain geometry was smaller than the lowest adiabatic energy, the diabatic energy was adjusted to coincide with the adiabatic energy. The amplitudes of the diabatic coupling constant were calculated from the interpolated surfaces. Its sign was taken from a direct interpolation of the defined coupling constants at the calculated points of the grid.

Appendix D: Calculation of ionization probability

The calculation of the structure dependent transition strength is motivated by work of Aberg[59,72,73]. Within the MC-SCF approach[41], electronic states Ψ can be expanded in a basis of Slater determinants ϕ_i as

$$\Psi = \sum_k c_k \phi_k, \tag{D1}$$

where c_k are CI coefficients. The Slater determinants can be expressed as a sequence of creation operators associated with the molecular orbitals (acting on the empty space)[74], resulting in expressions for the initial i and final states f

$$\Psi^i = \sum_k c_k \phi_k = \sum_k c_k \prod_{r=1}^{N} \left(\hat{a}_r^+\right)^{S_{r,k}} |\text{vac}\rangle \tag{D2}$$

$$\Psi^f = \sum_l c_l \phi_l = \sum_l c_l \prod_{r=1}^{N} \left(\hat{a}_r^+\right)^{S_{r,l}} |\text{vac}\rangle, \tag{D3}$$

where r runs over the number of (spin-)orbitals in the CI calculation and $S_{r,n}$ are the occupation-number vectors of the individual orbitals in the nth determinant. If we choose a biorthonormal basis, the operators are the same for the neutral and cationic molecule. We approximate the ionization probability within the sudden approximation as the norm of the Dyson orbital of the transition from state i to state f[60,61]

$$|\Phi_{if}|^2 = \left| \sum_q \left\langle \Psi^f \,\middle|\, \hat{a}_q \,\middle|\, \Psi^i \right\rangle \varphi_q \right|^2, \tag{D4}$$

where φ_q are the individual orbitals associated with the annihilation operators $\hat{a}_q$. Using the equations D2 and D3 this results in

$$\begin{aligned} |\Phi_{if}|^2 = \sum_q \Bigg| \sum_l \sum_k c_k c_l \\ \times \left\langle \text{vac} \left| \prod_{r=N}^{1} (\hat{a}_r)^{S_{r,l}} \hat{a}_q \prod_{r=1}^{N} \left(\hat{a}_r^+\right)^{S_{r,k}} \right| \text{vac} \right\rangle \Bigg|^2, \end{aligned} \tag{D5}$$

where we used the orthonormality of the individual orbitals φ_q. The bra-ket evaluates to ± 1 or 0, depending on the occupation of the initial state and the number of permutations needed to annihilate the qth electron from the initial state[74]. In practice, we evaluated equation D5 by calculating the state averaged electronic structure of the three lowest $^2\text{A}'$ states

with CASSCF(13,10) within the Molpro suite[40] and subsequently, while not optimizing the orbitals anymore, the three lowest cationic ^{1}A′, ^{1}A″, ^{3}A′, and ^{3}A″ states. All determinants with $c_k, c_l \geq 0.0001$ were included.

Appendix E: Calculation of expected experimental fs response

The femtosecond response illustrated in fig. 8b was caluclated similarly to a previously presented method[63]. The picosecond decay rates from jet-cooled NO_2[64] were interpolated to a function $k_{\mathrm{ps}}(E)$ with the excitation energy E. The expected bound population P_{B} after a broadband excitation was then calculated as

$$P_{\mathrm{B}}(E_{\mathrm{pump}}, t) = \int_E I_{\mathrm{pump}}(E, E_{\mathrm{pump}})\,(1 - \exp(-k_{\mathrm{ps}}(E)\,t))\,\mathrm{d}E, \tag{E1}$$

where I_{pump} describes the intensity spectrum of the excitation pulse. We assumed a Fourier-limited gaussian pulse centered at E_{pump} with a FWHM of 56 fs. Subsequent monoexponential fits to the population $P_{\mathrm{B}}(E_{\mathrm{pump}}, t)$ result in the energy-dependent femtosecond decay constants.

REFERENCES

[1] J. C. D. Brand, K. J. Cross, and A. R. Hoy, Can. J. Phys. **57**, 428 (1979).

[2] W. C. Bowman and F. C. D. Lucia, The Journal of Chemical Physics **77**, 92 (1982).

[3] A. Delon, R. Jost, and M. Jacon, The Journal of Chemical Physics **114**, 331 (2001).

[4] J. L. Hardwick and J. C. D. Brand, Canadian Journal of Physics **54**, 80 (1976).

[5] J. L. Hardwick and J. C. D. Brand, Chemical Physics Letters **21**, 458 (1973).

[6] R. Jost, J. Nygård, A. Pasinski, and A. Delon, J. Chem. Phys. **105**, 1287 (1996).

[7] R. Georges, A. Delon, and R. Jost, J. Chem. Phys. **103**, 1732 (1995).

[8] P. Baltzer, L. Karlsson, B. Wannberg, D. M. P. Holland, M. A. MacDonald, M. A. Hayes, and J. H. D. Eland, Chem. Phys. **237**, 451 (1998).

[9] G. K. Jarvis, Y. Song, C. Y. Ng, and E. R. Grant, The Journal of Chemical Physics **111**, 9568 (1999).

[10] A. T. J. B. Eppink, B. J. Whitaker, E. Gloaguen, B. Soep, A. M. Coroiu, and D. H. Parker, The Journal of Chemical Physics **121**, 7776 (2004).

[11]N. T. Form, B. J. Whitaker, L. Poisson, and B. Soep, Physical Chemistry Chemical Physics **8**, 2925 (2006).

[12]A. Vredenborg, W. G. Roeterdink, and M. H. M. Janssen, The Journal of Chemical Physics **128**, 204311 (2008).

[13]J.-B. Hamard, R. Cireasa, B. Chatel, V. Blanchet, and B. J. Whitaker, The Journal of Physical Chemistry A **114**, 3167 (2010).

[14]D. Irimia, I. D. Petsalakis, G. Theodorakopoulos, and M. H. Janssen, The Journal of Physical Chemistry A **114**, 3157 (2010).

[15]R. Forbes, A. E. Boguslavskiy, I. Wilkinson, J. G. Underwood, and A. Stolow, The Journal of Chemical Physics **147**, 054305 (2017).

[16]I. Wilkinson and B. J. Whitaker, Annu. Rep. Prog. Chem., Sect. C: Phys. Chem. **106**, 274 (2010).

[17]H. J. Wörner, J. B. Bertrand, D. V. Kartashov, P. B. Corkum, and D. M. Villeneuve, Nature **466**, 604 (2010).

[18]H. J. Wörner, J. B. Bertrand, B. Fabre, J. Higuet, H. Ruf, A. Dubrouil, S. Patchkovskii, M. Spanner, Y. Mairesse, V. Blanchet, E. Mével, E. Constant, P. B. Corkum, and D. M. Villeneuve, Science **334**, 208 (2011).

[19]P. M. Kraus, Y. Arasaki, J. B. Bertrand, S. Patchkovskii, P. B. Corkum, D. M. Villeneuve, K. Takatsuka, and H. J. Wörner, Phys. Rev. A **85**, 043409 (2012).

[20]H. Ruf, C. Handschin, A. Ferré, N. Thiré, J. B. Bertrand, L. Bonnet, R. Cireasa, E. Constant, P. B. Corkum, D. Descamps, B. Fabre, P. Larregaray, E. Mével, S. Petit, B. Pons, D. Staedter, H. J. Wörner, D. M. Villeneuve, Y. Mairesse, P. Halvick, and V. Blanchet, The Journal of Chemical Physics **137**, 224303 (2012).

[21]A. Tehlar and H. J. Wörner, Molecular Physics **111**, 2057 (2013).

[22]A. Tehlar, P. M. Kraus, and H. J. Wörner, Chimia **67**, 207 (2013).

[23]B. Liu, J. Zhu, B. Wang, Y. Wang, and L. Wang, The Journal of Physical Chemistry A **113**, 13839 (2009).

[24]A. von Conta, A. Tehlar, A. Schletter, Y. Arasaki, K. Takatsuka, and H. J. Wörner, submitted (2018).

[25]G. D. Gillispie, A. U. Khan, A. C. Wahl, R. P. Hosteny, and M. Krauss, J. Chem. Phys. **63**, 3425 (1975).

[26]C. F. Jackels and E. R. Davidson, J. Chem. Phys. **65**, 2941 (1976).

[27]C. F. Jackels and E. R. Davidson, J. Chem. Phys. **64**, 2908 (1976).

[28]G. Hirsch and R. J. Buenker, Can. J. Chem. **63**, 1542 (1985).

[29]H. Katagiri and S. Kato, J. Chem. Phys. **99**, 8805 (1993).

[30]S. Mahapatra, H. Köppel, L. S. Cederbaum, P. Stampfuss, and W. Wenzel, Chem. Phys. **259**, 211 (2000).

[31]D. Reignier, T. Stoecklin, P. Halvick, A. Voronin, and J. C. Rayez, Phys. Chem. Chem. Phys. **3**, 2726 (2001).

[32]V. Kurkal, P. Fleurat-Lessard, and R. Schinke, J. Chem. Phys. **119**, 1489 (2003).

[33]R. Schinke, S. Y. Grebenshchikov, and H. Zhu, Chem. Phys. **346**, 99 (2008).

[34]P. J. Fortune, B. J. Rosenberg, W. B. England, and A. C. Wahl, Theoretica chimica acta **46**, 183 (1977).

[35]D. M. Hirst, J. Chem. Phys. **115**, 9320 (2001).

[36]R. A. Kendall, T. H. Dunning Jr., and R. J. Harrison, J. Chem. Phys. **96**, 6796 (1992).

[37]Y. Arasaki and K. Takatsuka, Chem. Phys. **338**, 175 (2007).

[38]Y. Arasaki, K. Takatsuka, K. Wang, and V. McKoy, J. Chem. Phys. **132**, 124307 (2010).

[39]R. Islampour, M. Gharibi, and M. Miralinaghi, Molecular Physics **104**, 1879 (2006).

[40]H.-J. Werner, P. J. Knowles, G. Knizia, F. R. Manby, M. Schütz, *et al.*, "Molpro, version 2015.1, a package of ab initio programs," (2015).

[41]H.-J. Werner and P. J. Knowles, J. Chem. Phys. **82**, 5053 (1985).

[42]P. J. Knowles and H.-J. Werner, Chem. Phys. Lett. **115**, 259 (1985).

[43]H.-J. Werner and P. J. Knowles, J. Chem. Phys. **89**, 5803 (1988).

[44]P. J. Knowles and H.-J. Werner, Chem. Phys. Lett. **145**, 514 (1988).

[45]P. J. Knowles and H.-J. Werner, Theoretica Chimica Acta **84**, 95 (1992).

[46]G. Hirsch, R. J. Buenker, and C. Petrongolo, Mol. Phys. **70**, 835 (1990).

[47]A. Macías and A. Riera, J. Phys. B **11**, L489 (1978).

[48]M. S. Child, Mol. Phys. **72**, 89 (1991).

[49]M. D. Feit, J. A. Fleck, and A. Steiger, J. Comp. Phys. **47**, 412 (1982).

[50]K. Takatsuka and N. Hashimoto, J. Chem. Phys. **103**, 6057 (1995).

[51]J. Liévin, A. Delon, and R. Jost, J. Chem. Phys. **108**, 8931 (1998).

[52]G. C. Schatz and M. A. Ratner, *Quantum Mechanics in Chemistry* (Dover Inc., 2002).

[53]F. D. Sala, R. Rousseau, A. Görling, and D. Marx, Phys. Rev. Lett. **92**, 183401 (2004).

[54]M. Lax, J. Chem. Phys. **20**, 1752 (1952).

[55]S.-Y. Lee, R. C. Brown, and E. J. Heller, The Journal of Physical Chemistry **87**, 2045 (1983).

[56]S.-Y. Lee, The Journal of Chemical Physics **82**, 4588 (1985).

[57]M. K. Prakash, J. D. Weibel, and R. A. Marcus, Journal of Geophysical Research: Atmospheres **110**, D21315 (2005).

[58]O. Svoboda, L. Kubelová, and P. Slavíček, The Journal of Physical Chemistry A **117**, 12868 (2013).

[59]T. Åberg, Physical Review **156**, 35 (1967).

[60]G. Grell, S. I. Bokarev, B. Winter, R. Seidel, E. F. Aziz, S. G. Aziz, and O. Kühn, The Journal of Chemical Physics **145**, 089901 (2016).

[61]A. Ponzi, C. Angeli, R. Cimiraglia, S. Coriani, and P. Decleva, The Journal of Chemical Physics **140**, 204304 (2014).

[62]B. Kirmse, B. Abel, D. Schwarzer, S. Y. Grebenshchikov, and R. Schinke, The Journal of Physical Chemistry A **104**, 10398 (2000).

[63]B. Abel, S. Y. Grebenshchikov, R. Schinke, and D. Schwarzer, Chemical Physics Letters **368**, 252 (2003).

[64]S. I. Ionov, G. A. Brucker, C. Jaques, Y. Chen, and C. Wittig, J. Chem. Phys. **99**, 3420 (1993).

[65]D. Stolyarov, E. Polyakova, I. Bezel, and C. Wittig, Chemical Physics Letters **358**, 71 (2002).

[66]L. Nugent-Glandorf, M. Scheer, D. A. Samuels, A. M. Mulhisen, E. R. Grant, X. Yang, V. M. Bierbaum, and S. R. Leone, Phys. Rev. Lett. **87**, 193002 (2001).

[67]Y. Pertot, C. Schmidt, M. Matthews, A. Chauvet, M. Huppert, V. Svoboda, A. von Conta, A. Tehlar, D. Baykusheva, J.-P. Wolf, and H. J. Wörner, Science **355**, 264 (2017).

[68]Y. Arasaki, K. Wang, V. McKoy, and K. Takatsuka, Physical Chemistry Chemical Physics **13**, 8681 (2011).

[69]S. Scheit, Y. Arasaki, and K. Takatsuka, The Journal of Physical Chemistry A **116**, 2644 (2011).

[70]T. Matsuoka and K. Takatsuka, The Journal of Chemical Physics **146**, 134114 (2017).

[71]H. Akima, J. ACM **17**, 589 (1970).

[72]R. Manne and T. Åberg, Chem. Phys. Lett. **7**, 282 (1970).

[73]R. Arneberg, J. Müller, and R. Manne, Chemical Physics **64**, 249 (1982).

[74]T. Helgaker, P. Jørgensen, and J. Olsen, *Molecular Electronic-Structure Theory* (Wiley, 2013).